Published online 17 May 2023

Nucleic Acids Research, 2023, Vol. 51, No. 11 ***e65***
https://doi.org/10.1093/nar/gkad388

Accurate quantification of DNA using on-site PCR (osPCR) by characterizing DNA amplification at single-molecule resolution

Ruihua Ding[1,†], Liying Liu[2,†], Jiali Zhang[3,†], Pengxiao Lv[1], Lin Zhou[1], Tinglu Zhang[1], Shenwei Li[4], Ran Zhao[5], Zhuo Yang[3], Peng Xiong[2], Hu Chen[2], Wei Wang[4], Hualiang Wang[5], Zhengan Tian[4,*], Bo Liu[1,2,3,*] and Chang Chen[1,2,3,6,*]

[1]Shanghai Industrial μTechnology Research Institute (SITRI), Shanghai 201800, China, [2]Shanghai Si-Gene Biotech Co., Ltd, Shanghai 201800, China, [3]School of Microelectronics, Shanghai University, Shanghai 201800, China, [4]Shanghai International Travel Healthcare Center, Shanghai 200335, China, [5]Shanghai Center for Clinical Laboratory, Shanghai 200126, China and [6]State Key Laboratory of Transducer Technology, Shanghai Institute of Microsystem and Information Technology, Chinese Academy of Sciences, Shanghai 200050, China

Received January 17, 2023; Revised April 04, 2023; Editorial Decision April 25, 2023; Accepted May 01, 2023

ABSTRACT

Despite the need in various applications, accurate quantification of nucleic acids still remains a challenge. The widely-used qPCR has reduced accuracy at ultralow template concentration and is susceptible to nonspecific amplifications. The more recently developed dPCR is costly and cannot handle high-concentration samples. We combine the strengths of qPCR and dPCR by performing PCR in silicon-based microfluidic chips and demonstrate high quantification accuracy in a large concentration range. Importantly, at low template concentration, we observe on-site PCR (osPCR), where only certain sites of the channel show amplification. The sites have almost identical ct values, showing osPCR is a quasi-single molecule phenomenon. Using osPCR, we can measure both the ct values and the absolute concentration of templates in the same reaction. Additionally, osPCR enables identification of each template molecule, allowing removal of nonspecific amplification during quantification and greatly improving quantification accuracy. We develop sectioning algorithm that improves the signal amplitude and demonstrate improved detection of COVID in patient samples.

GRAPHICAL ABSTRACT

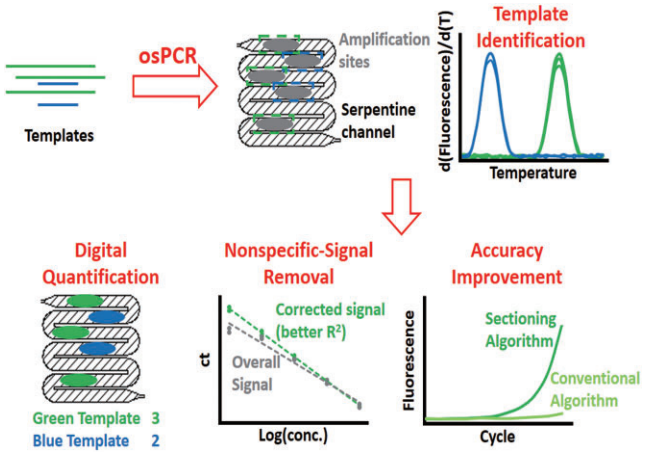

INTRODUCTION

Detection and quantification of specific nucleic acids is one of the most important procedures in both scientific research and medical diagnostics. As target nucleic acids are often related to a specific gene, individual or species, quantification of specific nucleic acids is a critical tool in areas including genotyping (1,2), forensics (3–6), prenatal diagnostics (7,8), and pathogen detection (9–11). The recent Corona Virus Disease 2019 (COVID) pandemic further illustrates the need for nucleic acid quantification, as the presence of the virus is often determined by the presence of viral RNA (12).

*To whom correspondence should be addressed. Tel: +86 021 62686286; Fax: +86 021 62686286; Email: tianzhenganciq@163.com
Correspondence may also be addressed to Bo Liu. Tel: +86 021 59918887; Fax: +86 021 59918887; Email: steven.liu@sitrigroup.com
Correspondence may also be addressed to Chang Chen. Tel: +86 021 66160096; Fax: +86 021 66160096; Email: chang.chen@mail.sim.ac.cn
†The authors wish it to be known that, in their opinion, the first three authors should be regarded as Joint First Authors.

Although multiple technologies have been developed, accurate quantification of target nucleic acid can still be challenging. PCR-based technologies are widely used for nucleic acid detection because of high sensitivity, high specificity and easiness in multiplexing. During the COVID pandemic, quantitative PCR (qPCR) is the gold standard of COVID viral RNA detection (12,13), despite the rapid development of novel testing methods including CRISPR-based assays (13–15), isothermal nucleotide amplification methods (16–18) and electrochemical assays (19,20). However, when the template concentration gets ultralow, quantification using the cycle threshold (ct) value from qPCR often become inaccurate (21,22), possibly due to qPCR instruments not sampling the whole reaction mixture. In addition, nonspecific amplification such as primer dimer formation can occur and the quantification result often has to be discarded when nonspecific amplification is detected. To accurately quantify trace amounts of DNA, digital PCR (dPCR) has been developed (23–27). However, dPCR is only accurate when the template is sufficiently dilute; thus it requires preknowledge of the sample concentration. In addition, dPCR is expensive and time-consuming. Overall, we still lack a method to quickly and accurately quantify target DNA, especially at ultralow template concentration.

Here, we report accurate quantification of DNA in a wide concentration range by performing PCR in silicon-based microfluidic chips. We perform ultrafast thermal cycling in the microfluidic chips and the performance is similar to conventional qPCR at high template concentrations. At ultralow template concentrations, our system shows localized amplification, where only certain 'sites' show fluorescent signals. By analysing the ct for each site and by comparing with conventional dPCR measurement, we confirm these amplification sites originate from single template molecules. The quasi-single molecule nature of these 'on-site PCR' enables distinguishing different templates in a mixed-template reaction. By identifying desired products from nonspecific products in the mixture, we can remove signals from nonspecific amplification during ct calculation and achieve accurate quantification of the desired template. We test our system on clinical samples and show osPCR-based sectioning algorithm enables more accurate identification of positive samples even when conventional qPCR gives ambiguous results.

MATERIALS AND METHODS

Microfluidic chip fabrication

The microfluidic chips are fabricated using 200 mm pilot line at SITRI using a workflow similar to previous studies (28). Briefly, SU-8 is used as photoresist to generate the pattern on double polished Si silicon wafer using photolithography. Microfluidic channels are fabricated using reactive ion etching. The wafer is cleaned with plasma and sulfuric acid. 400 μm-thick glass is used as the top layer. Holes on glass are made using laser drilling. The silicon and glass are then bonded using anodic bonding. After bonding, heat insulation regions are etched from the backside of silicon using photolithography followed by deep ion etching.

Thermal characterization

Simulation is performed using Comsol 5.6. The heating boundary conditions are set in the area of 1 cm × 1 cm. The thermal radiation boundary conditions are added to the external surface of the chip. The specific radiation loss ability is determined by the surface emissivity of the material. The finite element method (FEM) is used to solve the Fourier heat transfer equation of the microfluidic chip.

IR imaging is performed using MAG32 Infrared imager (Magnity Technologies, Shanghai, China).

osPCR

The rapid thermal cycling and imaging system is integrated as nucleic acid analyzer (SG-PCR-F001 or SG-PCR-MC16, Shanghai Si-Gene Biotech Co., Shanghai, China). In this work, only FAM channel is used and the exposure time is set at default 1s.

Unless noted otherwise, a typical PCR reaction has the final concentration of 0.2 μM primers each, 0.1 U/μl KAPA2G Fast HotStart PCR Enzyme (KAPA2G Fast HotStart PCR kit, Roche, Basel, Switzerland), 1x KAPA2G buffer supplemented with 0.5 mM Mg^{2+} and 0.2 mM dNTP. 0.8x Evagreen (Cat. 31000, Biotium, California, USA) is used as DNA dye.

The typical template we use is COVID S-Protein sequence 5'-TAGTGCTATTGGCAAAATTCAAGA CTCACTTTCTTCCACAGCAAGTGCACTTGG AAAACTTCAAGATGTGGTCAACCAAAATGC ACAAGCTTTAAACACGCTTGTTAAACAACTTA GCTCCAAT-3'. The short template sequence is 5'-GGCAAAATTCAAGACTCACTTTCTTCCACGCT TGTTAAACAACTTAGCTCCA-3'. The primers are 5'-GGCAAAATTCAAGACTCACTTTCTTCC-3' and 5'-TGGAGCTAAGTTGTTTAACAAGCGTG-3'. DNA strands are purchased from Genewiz (Suzhou, China).

Prepared PCR mix is added to the microfluidic chip by 10 μl pipetting tip through the inlet holes till the whole PCR channel got filled. Air escapes the chip from the exhaust channel. The injection holes are then sealed, typically using UV-curable adhesive (SL DZ200706A, Steady Chemical, Shanghai, China). Typical amplification cycle is 1 min at 95°C followed by 45 cycles of 2 s at 95°C and 15 s at 58°C. Following the amplification, an optional melting cycle from 65°C to 90°C may be performed with stepping size of 0.3°C.

Demonstration of localized PCR

The serial dilution shown in Figure 1 is performed using Novel Coronavirus (2019-nCoV) and influenza A/B Nucleic Acid Detection Kit (Z-RR-0488-02-50, Shanghai ZJ Bio-Tech, Shanghai, China). Plasmid with Influenza A sequence provided by Shanghai ZJ Bio-Tech is used as template. Amplification cycle is 45 s at 95°C followed by 45 cycles of 2 s at 95°C and 5 s at 60°C.

qPCR

Bulk qPCR for the model system is performed on SLAN-96P real-time PCR system (Hongshi, Shanghai, China) using the same reaction mix as osPCR. The thermal cycle

condition is 1 min at 95°C followed by 45 cycles of 2 s at 95°C and 15 s at 58°C. Melting cycle from 60°C to 90°C at 0.03°C/s is used to determine the melting temperature of products.

dPCR

Digital PCR is performed using QX200 (Bio-rad, CA, USA) machine. Instead of Evagreen, detection probe with sequence 5'-FAM-TCTTCCACAGCAAGTGCACT TGGA-BHQ1-3' is used. In addition to the negative control, the same sample is tested in 1×, 10× and 100× the concentration used in the lowest concentration for osPCR. After conversion, the average expected number is used as the dPCR measurement result.

Data analysis

Analysis is done using Python 3.8. Depending on the application, the fluorescence intensity may be determined in three algorithms.

1) Site algorithm. For each amplification site, we identify the whole region that the site spans and calculate the total fluorescence for the site. The background is removed by deducting the fluorescence by the average fluorescence of the cycles 5–15. After removing the background, the ct values are calculated using a fixed threshold.
2) Averaging algorithm. The whole microfluidic channel is identified and the fluorescence intensity of average of the whole channel is determined. If necessary, the signal of each site is determined using site algorithm and signal from unwanted sites, such as primer dimer sites, are removed before taking the average. After calculating the fluorescence intensity, the background is removed by deducting the fluorescence by the average fluorescence of the baseline cycles. For clinical samples amplified using kit Z-RR-0488–02-50 from Shanghai ZJ Bio-Tech, we use cycles 3–9 as baseline. The ct values are then calculated using a threshold of 10 times standard deviation of baseline cycles. For all other samples, we use cycles 5–15 as baseline unless the data show clear fluorescence increase before cycle 15. The ct values are then calculated using a fixed threshold.
3) Sectioning algorithm. The whole image is sectioned into equal-sized rectangular regions and the average fluorescence in each rectangle is calculated. For higher accuracy, we may try more than one way of sectioning. The fluorescence and ct values are calculated separately for each section using the same method as averaging algorithm. The region with the largest fluorescence change during amplification is used to represent the whole channel. Typically the result is regarded as positive as long as the fluorescence rises above threshold, giving a ct value.

Clinical samples

Clinical samples are obtained from Shanghai International Travel Healthcare Center (Shanghai Customs Port Clinic). All nasopharyngeal and oropharyngeal swabs samples are collected from incoming passengers who are formally notified and have signed the Informed Consent for Sampling. Samples are purified using Nucleic Acid Extraction System (SSNP-9600A, Jiangsu Bioperfectus Technologies, Taizhou, China) with Viral Nucleic Acid Extraction Kit (Magnetic Bead Method) (SDK60104, Jiangsu Bioperfectus Technologies, Taizhou, China) according to manufacturer's recommendation.

Bulk qPCR for clinical samples is performed using kits approved by Chinese National Medical Products Administration for Medical Instrument Registration Certificate on established qPCR machines according to manufacturer's recommendation. More specifically, we use COVID-19 Coronavirus Real Time PCR Kit (JC10223-1N, Jiangsu Bioperfectus Technologies, Taizhou, China) with thermal cycling condition of 10 min at 50°C, 1 min at 97°C followed by 45 cycles of 5 s at 97°C and 30 s at 58°C or novel coronavirus (2019-nCoV) Nucleic Acid Detection Kit (PCR-Fluorescence Probing) (ZC-HX-201–2, Shanghai BioGerm Medical Technology, Shanghai, China) with thermal cycling condition of 10 min at 50°C, 5 min at 95°C followed by 45 cycles of 10 s at 95°C and 40 s at 55°C on ABI QuantStudio 7 Flex (4485701, Thermo Fisher Scientific, USA) or LightCycler 480II (Roche, Basel, Switzerland).

For clinical samples frozen for less than 48 hours, PCRs in microfluidic chips are performed using Novel Coronavirus (2019-nCoV) and influenza A/B Nucleic Acid Detection Kit (Z-RR-0488–02-50, Shanghai ZJ Bio-Tech, Shanghai, China). Amplification cycle is 3 min at 50°C, 1 min at 95°C followed by 45 cycles of 1 s at 93°C and 5 s at 60°C. Images of the first 5 cycles are not taken. For clinical samples frozen for longer, PCRs in microfluidic chips are performed using COVID-19 Coronavirus Real Time PCR Kit (JC10223-1N, Jiangsu Bioperfectus Technologies, Taizhou, China) with thermal cycling condition of 10 min at 50°C, 1 min at 97°C followed by 45 cycles of 5 s at 97°C and 30 s at 58°C. We use up to the same amount of sample in qPCR to perform osPCR.

RESULTS

Rapid PCR using silicon-based microfluidic chips

We use silicon-based microfluidic chips as containers for PCR. The silicon chips have 500 μm-wide serpentine-shaped microfluidic channels in the reactor region to hold 6.5 μl PCR mixture during thermal cycling, and 100 μm-wide drain channels connecting to the inlets/outlets. Such design not only reduces the formation of bubbles during liquid loading, but also effectively confines the heat to the reactor region (28). In the reactor region, a chip typically has 4–16 microfluidic channels for PCR. Image of a 4-channel chip is shown in Figure 1A.

We perform rapid qPCR on microfluidic chips. The chips are rapidly heated and cooled using a custom-made Peltier heat pump. The Peltier heat pump and high thermal conductivity of silicon enable thermal cycling speed averaged at 20°C/s (max at 25°C/s), comparable to previously reported rapid PCR setups (Movie S1) (29–31). This ramping speed is much faster than conventional qPCR machines, which typically have average ramping speeds <5°C/s (data from websites of established qPCR machines including LightCyler 480II and Quantistudio 7 pro), saving time for our experiments. During thermal cycling, the thermal energy is

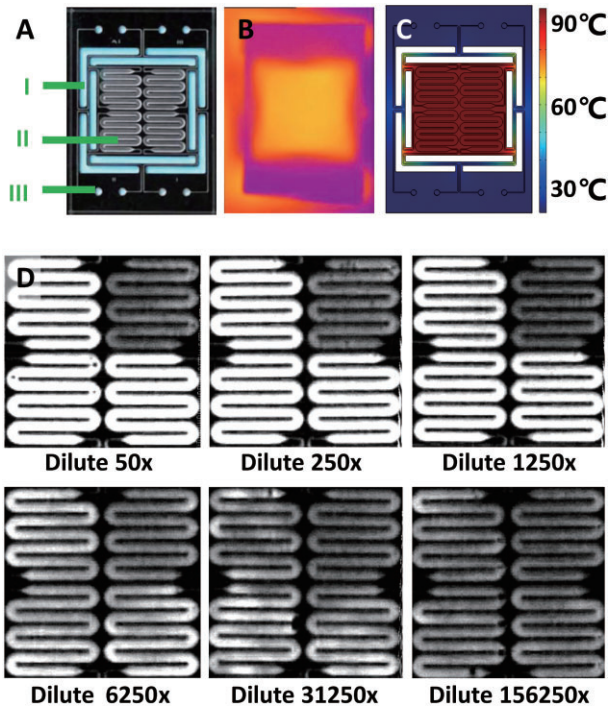

Figure 1. Silicon-based PCR microfluidic chip. (**A**) Bright field image of a 4-channel chip showing I. Drain channels with heat-insulation region; II. PCR channels in the reactor region; III. Sample inlet and outlet region. (**B**) Infrared image of 4-channel chip during heating and (**C**) numerical simulation of thermal profile of the chip during heating. Both (B) and (C) show localized heating effect. (**D**) Images of six chips with the template concentration serially diluted, showing uniform amplification at high template concentration and localized amplification at low template concentration. Images taken at the last thermal cycle. The top-right channels for each chip serve as negative controls.

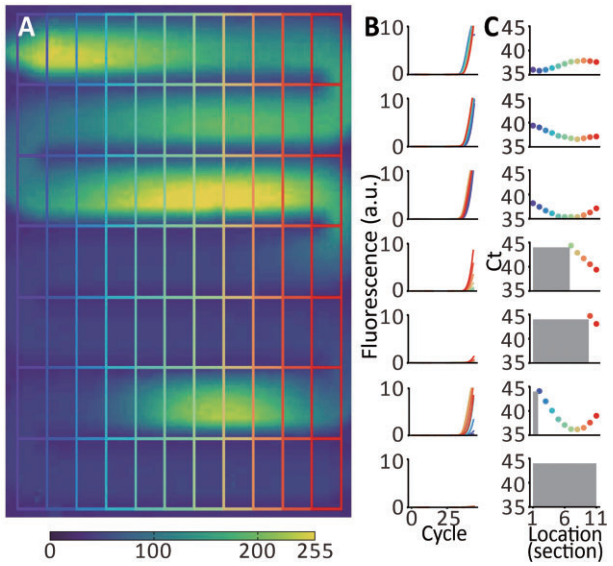

Figure 2. osPCR in microfluidic channels. (**A**) Image of a typical channel with localized amplification at last amplification cycle. The image is divided into different rectangular sections of the same area. (**B**) Fluorescence signal of the section in the corresponding row with the same color code. (**C**) The ct values of fluorescence curve in (B), plotted against the physical location in the channel for each row. Grey sections indicate the corresponding sections do not have enough fluorescence to have a ct value.

contained in the reactor region, as verified using both infrared imaging (Figure 1B, Movie S2) and numerical simulation (Figure 1C). During PCR, the chips are imaged using a side-illumination fluorescence optical setup (Figure S1). More detailed setup and characteristics of the system is reported before (32).

PCR occurs only at certain sites at low template concentration

We observe different fluorescence patterns during PCR amplification at different template concentrations. At high template concentration, the fluorescence is uniform. Interestingly, as template concentration decreases, we begin to observe localized PCR amplification in the microfluidic channels (Figure 1D). Such phenomena have been reported previously (28) but has not been thoroughly studied. We test various thermal cycle settings, enzymes and primer/template combinations for PCR in microfluidic channel; yet the localized amplification phenomenon is ubiquitous as long as the template is sufficiently dilute (Figure S2).

The localized amplification has patterns similar to a diffusion event. Certain locations of the channel give fluorescent signal first and the signal in the nearby regions follow. At the end of the amplification, the fluorescence is not uniform, and some regions of the channel may have no fluorescence. We divide the microfluidic channel region into multiple rectangular sections with the same area, and then measure the fluorescent signal in each section. Some, but not all, sections show fluorescent signals. Among the ones that show fluorescent signals, the ct values follow a smooth curve with the middle section having the lowest ct (Figure 2). We call this phenomenon 'on-site PCR' (osPCR) as the fluorescence in the channel is clustered to different 'sites'.

osPCR originates from amplification of single template molecules

The number of sites in each channel is correlated with the concentration of the template. We choose three different template concentrations and perform multiple reactions at each concentration. As the concentration increases, the average number of sites also increases. Furthermore, at each concentration, the distribution of the number of sites at each channel roughly resembles Poisson Distribution (Figure S3). This indicates that osPCR originates from uneven distribution of template molecules due to low concentration.

Interestingly, the sites have nearly identical ct values. We identify the region of each site and plot their fluorescence in each PCR cycle. The fluorescence curves have the signature exponential phase for qPCR and we determine the ct value for each site. Excitingly, nearly all the ct values from the sites on the same chip fall in a narrow range (Figures 3A–C, Figure S4). Such small variance in ct strongly indicates that each site has the same amount of templates. Considering some regions of the channel have no amplification, we hypothesize that osPCR is a quasi-single-molecule

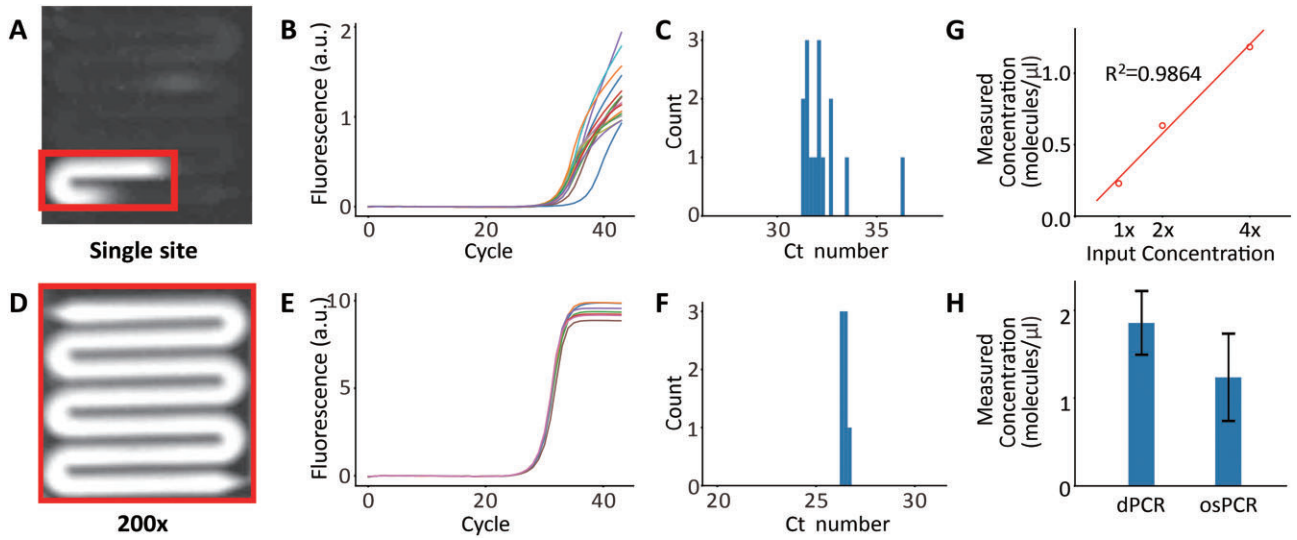

Figure 3. osPCR originates from localized PCR from single template molecules. (**A**) Fluorescence image of a microfluidic channel with one amplification site, highlighted in red rectangle. (**B**) Fluorescence curves for 15 amplification sites, including the region in (A). (**C**) histogram of ct values for curves in (B). (**D**) Fluorescence image of a channel with about 200x concentration than (A). (**E**) Fluorescence curves for seven channels with template concentration of (D). (**F**) Histogram of ct values for curves in (E). (**G**) Average template molecules measured using osPCR for three different input concentrations. (**H**) Comparison of measured absolute concentration for the same sample between dPCR and osPCR.

phenomenon and most of the sites originate from one template molecule.

The outliers among the site-ct values may be due to various stochastic events. We perform PCR at roughly 200 template molecules per channel and calculate the ct values for the whole channel. The resulting ct values are highly consistent, indicating there is no systematic bias in amplification (Figures 3E, F). Single-molecule events typically have higher inconsistency compared to bulk measurements, as observed in single molecule fluorescence (33), enzymatic activity (34), and plasmonics (35). In our case, we speculate that the sites with higher ct values are from template molecules in close proximity to the channel walls, where limited diffusion reduces the amplification efficiency in the initial cycles. For sites with lower ct, we believe they originate from multiple template molecules residing in close proximity. Two different sites in close proximity can merge by diffusion, resulting in a larger site in the final image (Figure S5). We assign the number of templates of each low-ct site based on the ct value.

To confirm that osPCR originates from quasi-single molecule amplification, we use osPCR to perform absolute quantification of templates. We perform osPCR of the same template at three different concentrations and count the number of templates in the channels. osPCR measurement results show strong linear correlation with the template concentration (Figure 3G). We then compare the number of templates measured using osPCR to the conventional gold standard dPCR. The resulting absolute concentrations from the two methods are comparable (Figure 3H, Figure S6). We attribute the slight discrepancy to pipetting error and DNA adhesion to pipette tips during serial dilution. These results strongly indicate that osPCR originates from quasi-single-template amplifications and can be used to measure the absolute concentration of template molecules.

osPCR enables identification of different templates in the same reaction

The quasi-single-molecule nature of osPCR enables distinguishing different template molecules. We design a 52 bp template and a 124 bp template with the same amplification primers. The two templates have distinct melting temperature (Tm). We mix the two templates in known molar ratios and perform osPCR followed by melting curve. We successfully obtain the melting curves from each site. Nearly all sites have only one Tm, either from the 124bp template (Figure 4, green) or from the 52 bp template (Figure 4, blue), allowing us to assign the site to either template. Only a few sites have two melting temperatures, likely due to both types of templates coincidentally residing in proximity to each other (Figure 4, purple, Movie S3). Furthermore, we are able to count the number of each template in each channel. We mix the two templates in two different molar ratios and perform PCR in 14 channels for each ratio. The resulting template amounts closely match the expected ratio for both mixing ratios we test (Table S1). This further confirms the capability of osPCR in distinguishing different templates and accurate quantification.

The capability of distinguishing different templates allows us to accurately quantify the template concentration in osPCR even in the presence of nonspecific amplifications such as primer dimers. We compare the performance of our microfluidic system and conventional qPCR at different template concentrations. At relatively high template concentrations, both systems obtain pure products and the ct values follow exponential relationship with template concentration. As the template concentration decreases, primer dimers appear. Conventional qPCR is capable of identifying samples with multiple melting points and the ct values from these samples are inaccurate because of primer dimers (Figure 5A, D). However, conventional qPCR lacks

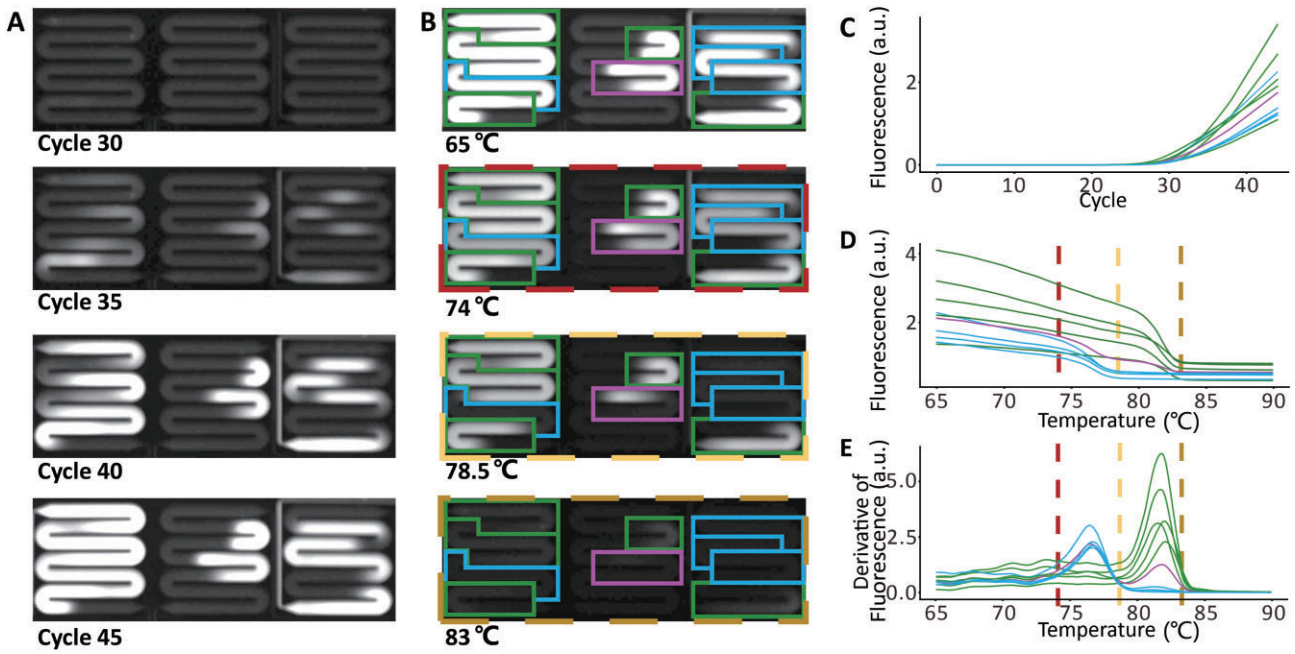

Figure 4. osPCR enables identification of different template molecules. (**A**) Images of three representative microfluidic channels at 30 cycles, 35 cycles, 40 cycles and 45 cycles of PCR. (**B**) Images of the same channels during melting curve at 65°C, 74°C, 78.5°C and 83°C. Sites with short, long and mixed templates are highlighted in blue, green and purple, respectively. (**C**) Amplification curve for each site shown with color code matching the highlight in (B). (**D**) fluorescence of each site during melting. (**E**) Melting curves of each site in the three microfluidic channels.

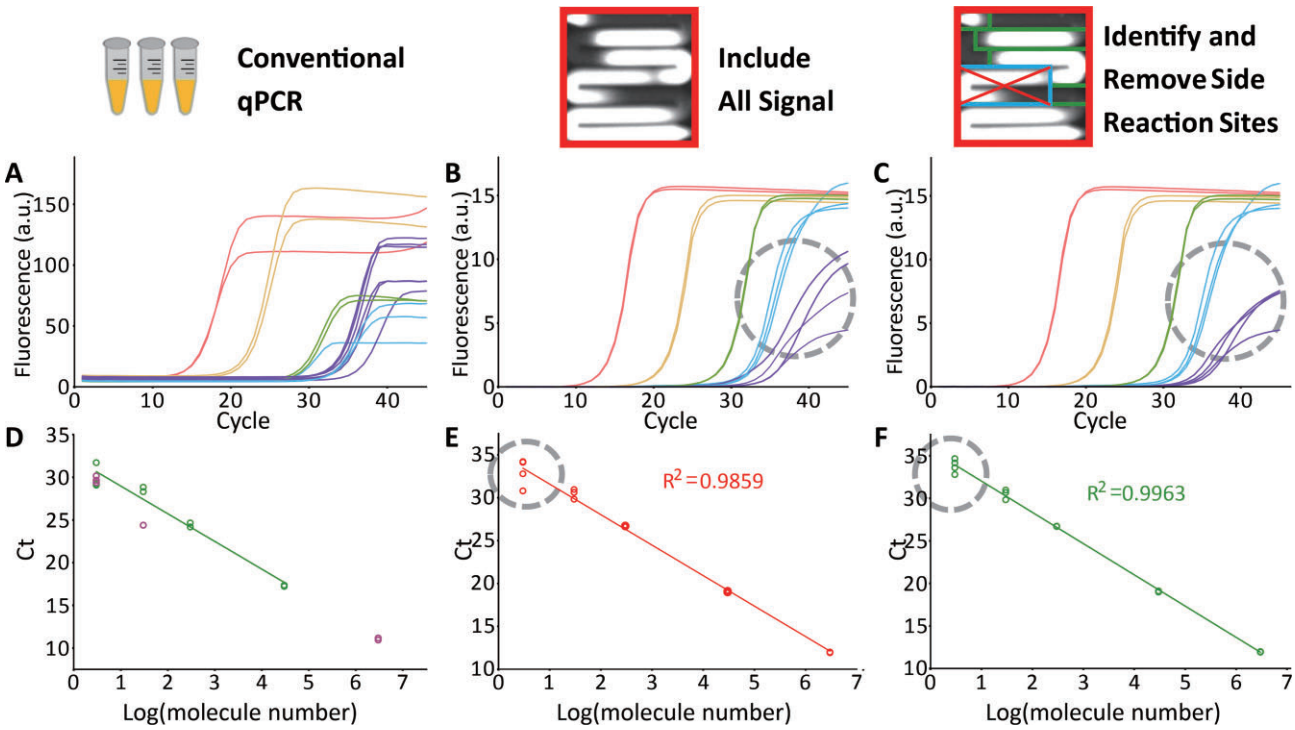

Figure 5. osPCR better quantifies template concentration. (**A**) Fluorescence curves for different template concentrations in conventional qPCR. (B, C) Amplification curves for different template concentrations in microfluidic channels without (**B**) or with (**C**) removal of primer dimer signal. Relative template concentrations are 1× (violet), 10× (blue), 100× (green), 10 000× (orange), and 1 000 000× (red). (**D**–**F**) Plot of ct values vs logarithm of template amount for (A–C), respectively. For (D), purple dots have more than one Tm and are not used for trendline calculation. Gray dashed circles highlight the effect of removing primer dimers using osPCR.

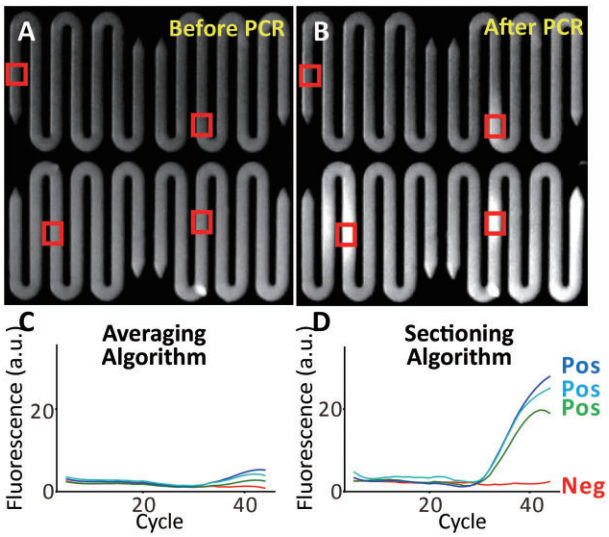

Figure 6. osPCR helps to identify positive results in clinical testing. (A, B) Same chip before (**A**) and after (**B**) PCR cycling. The top left channel has a negative sample while the other three channels contain positive samples. Red rectangles depict the region recognized using sectioning algorithm. (C, D) Fluorescence curve calculated from the chip using averaging algorithm (**C**) and sectioning algorithm (**D**).

the power to correct these ct numbers, leading to difficulty in accurately quantifying templates at low concentration. In contrast, in microfluidic system, we are able to identify the primer dimers by calculating the T_m from each amplification site. The sites identified as primer dimers can be dedicatedly removed by images analysis algorithm when calculating the fluorescence signal and the ct value. Such recalculated ct values closely follow the concentration trend and are more accurate (Figure 5). Therefore, our system is capable of precisely quantifying the template concentration even if there are undesired products.

osPCR improves identification of COVID-positive samples in clinical setting

To verify the performance of osPCR, we use our system to rapidly detect COVID in clinical setting. We test COVID ORF1ab in nasopharyngeal and oropharyngeal swabs samples from a total of 28 COVID-positive patients and 12 uninfected people. When testing with conventional qPCR machine with established protocols, one patient sample has ct higher than the manufacturer-recommended ct threshold and another patient sample is noted as 'ambiguous' from the qPCR machine. These issues during qPCR can lead to controversy in diagnostics and we aim to give more definitive results by identification of osPCR. To systematically identify positive samples with osPCR, we develop sectioning algorithm, where we dissect the images into equal-sized rectangular regions and only use the region with the strongest amplification signal for analysis, as they may be the center regions of osPCR sites (see Materials and Methods for details). The resulting amplification curves clearly distinguish positive and negative samples (Figure 6) and the ct for the same channel is drastically reduced compared to averaging algorithm (Table S2). Sectioning algorithm enhances the signal by only focusing on the region with strongest signals and determine whether amplification has occurred. Therefore sectioning algorithm cannot quantify the overall template concentration but is highly sensitive for detection assays. Using osPCR with sectioning algorithm, we clearly identify all 28 COVID-positive patient samples, including the two samples with ambiguous results from conventional qPCR, to be positive. Among the 12 negative samples, none show false positive result (Tables 1, S2). Therefore, our system gives reliable results in COVID testing in clinical settings and identification of osPCR improves the confidence in detecting low-concentration templates.

DISCUSSION

Although qPCR and dPCR have shown great success in nucleic acid quantification, improvement is still needed. For qPCR, the ct values are not directly related to absolute concentration. In addition, qPCR is often not accurate at ultralow template concentration. This might be because of conventional qPCR assumes the reaction mix is uniform and only measures the fluorescence in the lightpath. However, at ultralow concentration, the PCR reaction may not be uniform because, during the reaction, the products may not be homogeneously distributed in the tube. dPCR achieves accurate and absolute quantification of template molecules by compartmentalizing each template molecule in nanowells or droplets before performing PCR. Yet dPCR is not applicable for high template concentrations and the compartmentalization is often expensive and time-consuming.

Our work overcomes the limitations of qPCR and dPCR, providing a novel method for nucleic acid quantification. We measure the fluorescence in the whole microfluidic channel to avoid insufficient sampling of the reaction mixture. At low template concentration, we are able to count template molecules, achieving sensitivity and accuracy similar to dPCR. The imaging-based detection scheme also increases the accuracy of quantification by identification of nonspecific amplification, enabling quantification of template molecules at ultralow concentration or in contaminated samples. Furthermore, we are still able to accurately assign viable ct values for channels with down to one template molecule. In this way, our system directly links ct to absolute template concentration, bridging qPCR and dPCR.

Our system can be used for various applications. The capability of directly distinguishing template molecules at low concentration may be applied to applications such as testing nucleotide polymorphism and verifying mRNA alternative splicing. In addition, the osPCR-based sectioning algorithm improves the sensitivity of the platform for detection assays. The performance in COVID detection has demonstrated that our system can be applied in pathogen detection and point-of-care testing. The current system is low in throughput compared to the conventional qPCR machines, making it less suitable for large-scale screening experiment. However, increasing the throughput is not technically difficult. Overall, we believe this system can be widely applied for accurate detection and quantification of nucleic acids.

Table 1. Clinical samples tested with conventional qPCR and osPCR. Confusion matrixes for test results of 40 clinical samples tested using conventional qPCR and osPCR

	Conventional qPCR positive	Conventional qPCR negative or ambiguous		osPCR positive	osPCR negative
Actual positive	26	2	Actual positive	28	0
Actual negative	0	12	Actual negative	0	12

DATA AVAILABILITY

The authors declare that all data supporting the findings of this study are available within the paper and its supplementary information files. Requests for materials should be made to the corresponding author.

SUPPLEMENTARY DATA

Supplementary Data are available at NAR Online.

ACKNOWLEDGEMENTS

The authors thank SITRI Fab team for expedited silicon chip fabrication. The authors thank Shanghai ZJ Bio-Tech Co. for providing their COVID detection kit and plasmids.

FUNDING

Ministry of Science and Technology of the People's Republic of China [2021YFB3202504, 2022YFE0107400]; Science and Technology Commission of Shanghai Municipality [21NL2600100, 20DZ2220500]; Key Technology Team Project of Chinese Academy of Sciences [GJJSTD20210006]; SITRI and Si-gene Biotech Co., Ltd. Funding for open access charge: Ministry of Science and Technology of the People's Republic of China [2021YFB3202504].

Conflict of interest statement. The technology presented in this paper is the subject of pending or awarded patents filed by Si-Gene Biotech Co. Si-Gene Biotech Co. is a spin-off company from SITRI. B.L., C.C. and SITRI are shareholders of Si-Gene Biotech Co.

REFERENCES

1. Matsuda,K. (2017) PCR-based detection methods for single-nucleotide polymorphism or mutation: real-time PCR and its substantial contribution toward technological refinement. In: *Advances in Clinical Chemistry*. Academic Press Inc., Vol. **80**, pp. 45–72.
2. Ding,S., Chen,R., Chen,G., Li,M., Wang,J., Zou,J., Du,F., Dong,J., Cui,X., Huang,X. *et al.* (2019) One-step colorimetric genotyping of single nucleotide polymorphism using probe-enhanced loop-mediated isothermal amplification (PE-LAMP). *Theranostics*, **9**, 3723–3731.
3. Walker,J.A., Hedges,D.J., Perodeau,B.P., Landry,K.E., Stoilova,N., Laborde,M.E., Shewale,J., Sinha,S.K. and Batzer,M.A. (2005) Multiplex polymerase chain reaction for simultaneous quantitation of human nuclear, mitochondrial, and male Y-chromosome DNA: application in human identification. *Anal. Biochem.*, **337**, 89–97.
4. Swango,K.L., Timken,M.D., Chong,M.D. and Buoncristiani,M.R. (2006) A quantitative PCR assay for the assessment of DNA degradation in forensic samples. *Forensic Sci. Int.*, **158**, 14–26.
5. Jung,J.Y., Yoon,H.K., An,S., Lee,J.W., Ahn,E.R., Kim,Y.J., Park,H.C., Lee,K., Hwang,J.H. and Lim,S.K. (2018) Rapid oral bacteria detection based on real-time PCR for the forensic identification of saliva. *Sci. Rep.*, **8**, 2–11.
6. Fu,J. and Allen,R.W. (2019) A method to estimate the age of bloodstains using quantitative PCR. *Forensic Sci. Int. Genet.*, **39**, 103–108.
7. Lo,Y.M.D., Tein,M.S.C., Lau,T.K., Haines,C.J., Leung,T.N., Poon,P.M.K., Wainscoat,J.S., Johnson,P.J., Chang,A.M.Z. and Hjelm,N.M. (1998) Quantitative analysis of fetal DNA in maternal plasma and serum: implications for noninvasive prenatal diagnosis. *Am. J. Hum. Genet*, **62**, 768–775.
8. Traeger-Synodinos,J. (2006) Real-time PCR for prenatal and preimplantation genetic diagnosis of monogenic diseases. *Mol. Aspects Med.*, **27**, 176–191.
9. Kamau,E., Alemayehu,S., Feghali,K.C., Saunders,D. and Ockenhouse,C.F. (2013) Multiplex qPCR for detection and absolute quantification of malaria. *PLoS One*, **8**, e91539
10. Kodani,M., Yang,G., Conklin,L.M., Travis,T.C., Whitney,C.G., Anderson,L.J., Schrag,S.J., Taylor,T.H., Beall,B.W., Breiman,R.F. *et al.* (2011) Application of TaqMan low-density arrays for simultaneous detection of multiple respiratory pathogens. *J. Clin. Microbiol.*, **49**, 2175–2182.
11. Zhang,H., Nie,K., Liu,Y., Luo,L., Huang,W., Zhou,S., Yang,M., Chen,Y., Luo,J., Gao,L. *et al.* (2012) Evaluation of reverse transcription loop-mediated isothermal amplification assays for rapid detection of human enterovirus 71 and coxsackievirus A16 in clinical samples. *Adv. Infect. Dis.*, **02**, 110–118.
12. WHO (2021) Recommendations for national SARS-Cov-2 testing strategies and diagnostic capacities. World Health Organization, Vol. **1**, pp. 1–16.
13. Ding,X., Yin,K., Li,Z., Lalla,R.V., Ballesteros,E., Sfeir,M.M. and Liu,C. (2020) Ultrasensitive and visual detection of SARS-CoV-2 using all-in-one dual CRISPR-Cas12a assay. *Nat. Commun.*, **11**, 4711
14. Broughton,J.P., Deng,X., Yu,G., Fasching,C.L., Servellita,V., Singh,J., Miao,X., Streithorst,J.A., Granados,A., Sotomayor-Gonzalez,A. *et al.* (2020) CRISPR–Cas12-based detection of SARS-CoV-2. *Nat. Biotechnol.*, **38**, 870–874.
15. Fozouni,P., Son,S., Díaz de León Derby,M., Knott,G.J., Gray,C.N., D'Ambrosio,M.V., Zhao,C., Switz,N.A., Kumar,G.R., Stephens,S.I. *et al.* (2021) Amplification-free detection of SARS-CoV-2 with CRISPR-Cas13a and mobile phone microscopy. *Cell*, **184**, 323–333.
16. Zhang,C., Zheng,T., Wang,H., Chen,W., Huang,X., Liang,J., Qiu,L., Han,D. and Tan,W. (2021) Rapid one-pot detection of SARS-CoV-2 based on a lateral flow assay in clinical samples. *Anal. Chem.*, **93**, 3325–3330.
17. Rodriguez-Manzano,J., Malpartida-Cardenas,K., Moser,N., Pennisi,I., Cavuto,M., Miglietta,L., Moniri,A., Penn,R., Satta,G., Randell,P. *et al.* (2021) Handheld point-of-care system for rapid detection of SARS-CoV-2 extracted RNA in under 20 min. *ACS Cent. Sci.*, **7**, 307–317.
18. Cherkaoui,D., Huang,D., Miller,B.S., Turbé,V. and McKendry,R.A. (2021) Harnessing recombinase polymerase amplification for rapid multi-gene detection of SARS-CoV-2 in resource-limited settings. *Biosens. Bioelectron.*, **189**, 113328
19. Wang,L., Wang,X., Wu,Y., Guo,M., Gu,C., Dai,C., Kong,D., Wang,Y., Zhang,C., Qu,D. *et al.* (2022) Rapid and ultrasensitive electromechanical detection of ions, biomolecules and SARS-CoV-2 RNA in unamplified samples. *Nat. Biomed. Eng.*, **6**, 276–285.
20. Zhao,H., Zhang,Y., Chen,Y., Ho,N.R.Y., Sundah,N.R., Natalia,A., Liu,Y., Miow,Q.H., Wang,Y., Tambyah,P.A. *et al.* (2021) Accessible detection of SARS-CoV-2 through molecular nanostructures and automated microfluidics. *Biosens. Bioelectron.*, **194**, 113629.
21. Tahamtan,A. and Ardebili,A. (2020) Real-time RT-PCR in COVID-19 detection: issues affecting the results. *Expert Rev. Mol. Diagn.*, **20**, 453–454.
22. Yin,H., Wu,Z., Shi,N., Qi,Y., Jian,X., Zhou,L., Tong,Y., Cheng,Z., Zhao,J. and Mao,H. (2021) Ultrafast multiplexed detection of

SARS-CoV-2 RNA using a rapid droplet digital PCR system. *Biosens. Bioelectron.*, **188**, 113282
23. Taylor,S.C., Laperriere,G. and Germain,H. (2017) Droplet Digital PCR versus qPCR for gene expression analysis with low abundant targets: from variable nonsense to publication quality data. *Sci. Rep.*, **7**, 2409.
24. Suo,T., Liu,X., Feng,J., Guo,M., Hu,W., Guo,D., Ullah,H., Yang,Y., Zhang,Q., Wang,X. *et al.* (2020) ddPCR: a more accurate tool for SARS-CoV-2 detection in low viral load specimens. *Emerg. Microbes Infect.*, **9**, 1259–1268.
25. Sanders,R., Huggett,J.F., Bushell,C.A., Cowen,S., Scott,D.J. and Foy,C.A. (2011) Evaluation of digital PCR for absolute DNA quantification. *Anal. Chem.*, **83**, 6474–6484.
26. Hindson,C.M., Chevillet,J.R., Briggs,H.A., Gallichotte,E.N., Ruf,I.K., Hindson,B.J., Vessella,R.L. and Tewari,M. (2013) Absolute quantification by droplet digital PCR versus analog real-time PCR. *Nat. Methods*, **10**, 1003–1005.
27. Hindson,B.J., Ness,K.D., Masquelier,D.A., Belgrader,P., Heredia,N.J., Makarewicz,A.J., Bright,I.J., Lucero,M.Y., Hiddessen,A.L., Legler,T.C. *et al.* (2011) High-throughput droplet digital PCR system for absolute quantitation of DNA copy number. *Anal. Chem.*, **83**, 8604–8610.
28. Cai,Q., Fauvart,M., Wiederkehr,R.S., Jones,B., Cools,P., Goos,P., Vaneechoutte,M. and Stakenborg,T. (2019) Ultra-fast, sensitive and quantitative on-chip detection of group B streptococci in clinical samples. *Talanta*, **192**, 220–225.
29. Neuzil,P., Zhang,C., Pipper,J., Oh,S. and Zhuo,L. (2006) Ultra fast miniaturized real-time PCR: 40 cycles in less than six minutes. *Nucleic Acids Res.*, **34**, e77
30. Wu,J., Jiang,K., Mi,H., Qiu,Y., Son,J., Park,H.J., Nam,J.M. and Lee,J.H. (2021) A rapid and sensitive fluorescence biosensor based on plasmonic PCR. *Nanoscale*, **13**, 7348–7354.
31. Kim,H., Vishniakou,S. and Faris,G.W. (2009) Petri dish PCR: laser-heated reactions in nanoliter droplet arrays. *Lab Chip*, **9**, 1230–1235.
32. Zhang,J., Yang,Z., Liu,L., Zhang,T., Hu,L., Hu,C., Chen,H., Ding,R., Liu,B. and Chen,C. (2023) Ultrafast nucleic acid detection equipment with silicon-based microfluidic chip. *Biosensors*, **13**, 234.
33. Luo,G., Wang,M., Konigsberg,W.H. and Xie,X.S. (2007) Single-molecule and ensemble fluorescence assays for a functionally important conformational change in T7 DNA polymerase. *Proc. Natl. Acad. Sci. U.S.A.*, **104**, 12610–12615.
34. Min,W., English,B.P., Luo,G., Cherayil,B.J., Kou,S.C. and Xie,X.S. (2005) Fluctuating enzymes: lessons from single-molecule studies. *Acc. Chem. Res.*, **38**, 923–931.
35. Chen,C., Li,Y., Kerman,S., Neutens,P., Willems,K., Cornelissen,S., Lagae,L., Stakenborg,T. and Van Dorpe,P. (2018) High spatial resolution nanoslit SERS for single-molecule nucleobase sensing. *Nat. Commun.*, **9**, 1733